

Laser-controlled vibrational heating and cooling of oriented H_2^+ molecules

This article has been downloaded from IOPscience. Please scroll down to see the full text article.

2012 J. Phys. B: At. Mol. Opt. Phys. 45 105602

(<http://iopscience.iop.org/0953-4075/45/10/105602>)

View [the table of contents for this issue](#), or go to the [journal homepage](#) for more

Download details:

IP Address: 129.130.106.65

The article was downloaded on 03/05/2012 at 17:51

Please note that [terms and conditions apply](#).

Laser-controlled vibrational heating and cooling of oriented H_2^+ molecules

Thomas Niederhausen¹, Uwe Thumm² and Fernando Martín^{1,3}

¹ Departamento de Química, Módulo 13, Universidad Autónoma de Madrid, 28049 Madrid, Spain

² James R Macdonald Laboratory, Kansas State University, Manhattan, KS 66506-2604, USA

³ Instituto Madrileño de Estudios Avanzados en Nanociencia (IMDEA-Nanociencia), Cantoblanco, 28049 Madrid, Spain

E-mail: thomas.niederhausen@uam.es, thumm@phys.ksu.edu and fernando.martin@uam.es

Received 19 January 2012, in final form 13 March 2012

Published 2 May 2012

Online at stacks.iop.org/JPhysB/45/105602

Abstract

We investigate the control of the vibrational dynamics in the hydrogen molecular ion H_2^+ using strong femto-second infrared control-laser pulses. For our three-dimensional calculations, we use infrared laser pulses of 800 nm wavelength, 6 fs pulse duration and a peak intensity between 10^{12} and 10^{15} W cm^{-2} . For laser electric fields aligned along the molecular axis, we numerically solve the full vibronic Schrödinger equation and compare our results with a model calculation that only includes the nuclear motion on the two lowest coupled adiabatic Born–Oppenheimer potential curves. The initial vibrational wave packet is launched with the ionization of the parent H_2 molecule in the pump pulse. Precise timing between pump- and control-laser pulses allows for the direct manipulation of the final bound vibrational-state composition and dissociation dynamics of the ion. We show that significant enhancement of the occupation of particular stationary vibrational-state contributions can be achieved for laser intensities below the onset of strong ionization ($\approx 10^{14}$ W cm^{-2}). In addition, we find that this vibrational selectivity strongly depends on the delay time but not on the intensity of the control pulse. The *relative* stationary vibrational-state contributions and the shape of the vibrating wave packet depend sensitively on the control-pulse delay time, and the overall amplitude of the final vibrational wave packet depends on the intensity of the control pulse.

(Some figures may appear in colour only in the online journal)

1. Introduction

The *ab initio* description of the hydrogen molecular ion in strong laser fields is complex and involves two distinct timescales for the electronic and nuclear dynamics. Nevertheless, the molecular hydrogen ion and its heavier isotopes have been studied extensively, both experimentally and theoretically, due to their benchmarking character as the simplest molecule [1, 2]. Albeit being the smallest molecular system consisting of just three charged particles, nearly exact solutions of the time-dependent Schrödinger equation (TDSE) including all electronic and nuclear degrees of freedom have only become accessible within the last decade [3, 4]. Such full-dimensionality (3D) calculations are of particular importance if the laser-driven molecular dynamics includes dissociation

which is sensitive to the coupled electronic and the nuclear motion.

A computationally less demanding method is the adiabatic close-coupling approach in which the nuclear dynamics is limited to the lowest few adiabatic molecular states. This method was used, e.g., to investigate the effect of strong IR laser pulses on the dissociation dynamics and final vibrational-state distribution in H_2^+ [5] and to describe the ionization of H_2^+ by ultraviolet light pulses [6]. However, for large laser intensities, close-coupling methods so far have been impractical, since their convergence requires a large number of adiabatic molecular states, making such calculations prohibitively expensive. In this case, truncation of the close-coupling expansion can lead to inaccurate results. This has been demonstrated, e.g., in [7], where the observed dissociation probability differs quantitatively

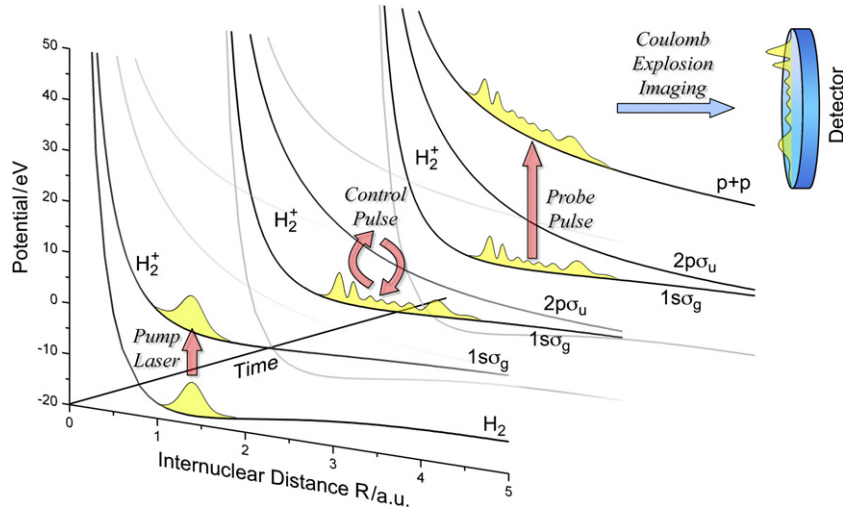


Figure 1. Simplified pump–control–probe scheme corresponding to a two-state Born–Oppenheimer (BO) model for the nuclear motion in H_2^+ . The pump-laser pulse ionizes the neutral H_2 molecule, launching a nuclear vibrational wave packet in the H_2^+ ion. A subsequent control pulse modifies the vibrational-state distribution of the ion by inducing Raman transitions between the $1s_g$ and $2p_u$ electronic states at a given delay time. Finally, the vibrational state is probed destructively by dissociation or Coulomb explosion in the probe-laser pulse. The ‘3D calculations’ discussed in this work accurately include excited electronic and vibrational levels (not shown) beyond the BO approximation.

from that obtained in earlier close-coupling calculations [5]. In addition, the adiabatic approximation (with which we mean the exclusion of all non-laser-induced couplings between adiabatic molecular electronic states) breaks down near avoided crossings and conical intersections of potential energy curves (surfaces) [8, 9].

Modern computational resources have allowed theoretical descriptions of the coupled nuclear–electronic dynamics, including non-adiabatic effects [3, 4, 10–13], for a series of interesting applications. One such example is the proposed [11] and recently observed control over the left–right asymmetry in the electron localization of dissociating H_2^+ [14] and D_2^+ [15] ions with few-cycle carrier-envelope-phase-stabilized laser pulses. In this paper, we present an implementation of a 3D method to solve the TDSE by using cylindrical coordinates. We apply it to the study of the nuclear motion in the hydrogen molecular ion H_2^+ that is generated by a pump-laser pulse from the H_2 parent molecule. After a certain delay time, a short, intense control-laser pulse induces transitions between the $1s_g$ and $2p_u$ molecular ion states, changing the vibrational-state composition of the bound nuclear wave packet in the $1s_g$ adiabatic potential well of the molecular ion. This allows for the coherent control of the quantum system, e.g., the quenching of the vibrational-state distribution or stopping of the nuclear wave packet [16, 17]. Through a third, intense probe pulse, the resulting vibrational wave packet can then be analysed using Coulomb-explosion imaging [18–20]. The schematics of this pump–probe–control scheme is shown in figure 1.

For a similar pump–control–probe-pulse scheme, an alternating population of odd and even final vibrational states has been predicted theoretically [21] by applying the control pulse near a fractional revival time [22] of the nuclear wave packet in D_2^+ . A semi-classical model, in which the nuclear wave packet is approximated by a classical ensemble of particles moving on the Stark-shifted $1s_g$ potential energy

surface, has been applied to describe the final vibrational-state population [23, 24]. So far, the proposed vibrational control schemes have been confirmed experimentally only with regard to the dissociation yield [25, 26] and electron localization during dissociation [26, 27]. Thus, at this stage, it is timely to investigate control within a pump–control–probe-pulse scheme of the nuclear motion in H_2^+ in accurate quantum mechanical calculations. For this purpose, we have developed a new computational code and performed a sequence of calculations for the interaction of H_2 with ultrashort intense pump, control and probe pulses. We will refer to these computations as ‘3D calculation’ throughout this work and compare our 3D results with theoretical predictions obtained previously within a simplified two-state model (TSM) [16].

If not specified otherwise, atomic units will be used throughout this work ($e = \hbar = m_e = 1$).

2. Theory

2.1. Full-dimensional calculations

The full non-relativistic field-free Hamiltonian for the hydrogen molecular ion H_2^+ in the body-fixed reference frame, representing the two nuclei with relative position vector \mathbf{R} and the single electron at position \mathbf{r} relative to the centre of mass of the two nuclei, is given by

$$\hat{H}_0 = -\frac{1}{2M} \frac{d^2}{d\mathbf{R}^2} - \frac{1}{2\mu_e} \frac{d^2}{d\mathbf{r}^2} + \frac{1}{R} - \frac{1}{|\mathbf{r} + \frac{\mathbf{R}}{2}|} - \frac{1}{|\mathbf{r} - \frac{\mathbf{R}}{2}|}. \quad (1)$$

$M = 918.076$ is the reduced mass of the two nuclei [28], and $\mu_e = 2M/(2M + 1)$ the reduced mass of the electron. We can restrict our calculations to molecules that are aligned with respect to the laser-electric-field vector and therefore neglect molecular rotation [3, 4, 29]. Aligned molecular ions can

be selected *a posteriori* in coincidence experiments [30, 31]. Thus, including all electronic degrees of freedom and taking advantage of the cylindrical symmetry of the potential, two degrees of freedom remain for the electronic motion along the internuclear axis z and the radial distance ρ from the molecular axis. Including the internuclear separation R , the time-independent Hamiltonian (1) becomes

$$\hat{H}_0 = -\frac{1}{2M} \frac{\partial^2}{\partial R^2} - \frac{1}{2\mu_e} \left(\frac{\partial^2}{\partial \rho^2} + \frac{\partial}{\partial \rho} \frac{1}{\rho} + \frac{\partial^2}{\partial z^2} \right) + V_0, \quad (2)$$

where the field-free molecular potential $V_0 = V_0(R, \rho, z)$ is given by

$$V_0 = \frac{1}{R} - \frac{1}{\sqrt{\rho^2 + (z - R/2)^2}} - \frac{1}{\sqrt{\rho^2 + (z + R/2)^2}}. \quad (3)$$

The external laser electric field is aligned with the internuclear axis and is characterized by the envelope function

$$f(t) = \begin{cases} E_0 \cos^2 \left(\frac{\pi(t - t_0)}{\beta\tau} \right) & |t - t_0| \leq \frac{\beta\tau}{2} \\ 0 & \text{otherwise,} \end{cases} \quad (4)$$

where τ is the pulse width. The factor $\beta = \pi/(2 \arccos 2^{-1/4}) = 2.747$ is introduced so that τ represents the FWHM (full-width at half-maximum) of the pulse intensity. It converts the FWHM pulse width in the intensity to the electric field. The oscillating field of the laser pulse with the central frequency ω and the peak intensity $I_0 = E_0^2$ can be written as

$$E(t) = f(t) \cos \omega(t - t_0). \quad (5)$$

The resulting time-dependent external potential in the dipole-length gauge is

$$V_L(z, t) = zE(t). \quad (6)$$

For the setup described above, the 3D TDSE for the interaction of the molecular ion with the external laser field can be written as

$$\left(\hat{H}_0 + V_L(z, t) - i \frac{\partial}{\partial t} \right) \Psi(R, \rho, z, t) = 0. \quad (7)$$

We represent the wavefunction and operators on a numerical lattice. The Coulomb singularity at either nucleus in (3) is avoided by locating the first lattice point in ρ -direction at $1/2$ of the grid spacing, thereby eliminating the need of a softening parameter. Utilizing a non-equidistant (cubic) grid with smaller grid spacings near the nuclei, we further reduce the numerical effort without sacrificing accuracy in representing bound electronic states. For a one-dimensional scenario, the kinetic energy operator $\hat{T} = \hat{p}^2/2m$ in coordinate space for an arbitrary numerical grid can be represented by a tridiagonal matrix [32], while the potentials (3) and (6) result in a diagonal matrix.

Let $\psi_n(R, \rho, z)$ be the n th bound vibronic eigenstate of H_2^+ . The probability for finding the system in this state is obtained by projecting $\Psi(R, \rho, z, t)$ onto the former state,

$$P_n^{3D}(t) = |\langle \psi_n(R, \rho, z) | \Psi(R, \rho, z, t) \rangle|^2. \quad (8)$$

The vibronic wavefunctions $\psi_n(R, \rho, z)$ are obtained by the diagonalization of the full field-free Hamiltonian (2). For this diagonalization we take advantage of the sparsity of the

Hamiltonian matrix. In our three-point discretization of the kinetic energy operators the Hamiltonian matrix is composed of a diagonal band containing seven lines. The main diagonal contains the potential contribution. The off-diagonal lines arise from coupling through the kinetic energy operator to its nearest neighbours in all three coordinate directions, i.e. one off-diagonal line on each side of the diagonal per coordinate. We solve this time-independent eigenvalue problem using the PETSc [33] and SLEPc [34] routines that are optimized for parallel processing. For the lowest 15 vibrational bound states of the hydrogen molecular ion, we obtained converged results with a ground-state energy of $E_0 = -0.604$, which is slightly below the accepted Born–Oppenheimer (BO) value of -0.597 [35].

For the time propagation, we solve the TDSE (7) using the Crank–Nicolson scheme [36, 37] with an operator-splitting scheme that minimizes the numerical expense by symmetrically dividing the numerically less demanding potential operation,

$$\Psi(R, \rho, z, t + \Delta t) = e^{-iV\Delta t/2} e^{-i\hat{T}_R\Delta t} e^{-i\hat{T}_\rho\Delta t} \times e^{-i\hat{T}_z\Delta t} e^{-iV\Delta t/2} \Psi(R, \rho, z, t) + \mathcal{O}(\Delta t^3). \quad (9)$$

Our three-dimensional grid spans a total of 30 au in R -direction and 80 au \times 40 au in the $z \times \rho$ plane with a minimum grid spacing of $\Delta_R = 0.05$ and $\Delta_\rho = \Delta_z = 0.1$. These grid spacings gradually increase towards the outer grid boundaries. The time step for the electronic propagation is $\Delta t_{\text{elec}} = 0.015$ and for the nuclear propagation, which we only perform every ten electronic time steps, $\Delta t_{\text{nucl}} = 0.15$. This results in the stability parameters [36] $\mu_{\text{elec}} = \Delta t / (2\mu_e (\Delta\rho)^2) = \Delta t / (2\mu_e (\Delta z)^2) \leq 0.75$ and $\mu_{\text{nucl}} = \Delta t / (2M (\Delta R)^2) \leq 0.033$. Both parameters are smaller than 1 and guarantee the numerical accuracy of the propagation scheme.

Wavefunction absorbers are used at the outer grid boundaries to suppress reflections and are implemented in terms of quadratic masking functions. For example, the absorption in the X -direction (with X being R , ρ or z) beyond the point X_0 until the end of the grid X_{max} invokes the masking function $a(X) = \exp[-s_X ((X - X_0)/(X_{\text{max}} - X_0))^2]$ which is applied every time step with the absorption strength parameter s_X (with $s_\rho = s_z = 1$ for the electronic and $s_R = 0.1$ for the nuclear absorber). For our calculations we use 10 au for the length of the nuclear and 20 au for the electronic absorbers in the ρ - and z -directions and adjusted both, the nuclear and electronic strength parameter, to obtain converged results with the parameters given above. We have verified the convergence of the propagated wavefunction by using absorbers of twice the width and by modifying values of the absorption strength parameters s_X .

2.2. Adiabatic TSM

We expand the solution of the TDSE (7) in terms of a BO basis set

$$\Psi(R, \rho, z, t) = \sum_{i,n} a_{in}(t) \chi_{in}(R) \varphi_i(R; \rho, z) e^{-iE_{in}t}, \quad (10)$$

where $\varphi_i(R; \rho, z)$ are the electronic states parametric in R , $\chi_{in}(R)$ are the nuclear states, E_{in} are the corresponding energies

and $a_{in}(t)$ are the time-dependent expansion coefficients. By writing (10) as a summation and integration we allow for the general case where the electronic-state label i and the vibronic quantum number n can represent both, discrete bound and continuum states.

We will compare the results from our 3D calculations with solutions obtained by truncating the expansion (10). For this purpose, we adopt the coupled adiabatic TSM from our previous work [16], which only includes the lowest two electronic states of the molecule,

$$\left(\hat{T} + V(R) + \hat{H}_c(R) - i \frac{\partial}{\partial t} \right) \begin{pmatrix} \chi_g(R, t) \\ \chi_u(R, t) \end{pmatrix} = 0. \quad (11)$$

In this model, a nuclear wave packet moves on the coupled $1s\sigma_g$ and $2p\sigma_u$ potential curves

$$V(R) = \begin{pmatrix} V_g(R) & 0 \\ 0 & V_u(R) \end{pmatrix}. \quad (12)$$

Both nuclear potential curves are obtained on the basis of one-electron diatomic molecular orbitals, which give the exact solutions of the single-electron two-centre Hamiltonian [38]. The set of bound vibrational eigenfunctions $\chi_{g,n}(R)$ on the $V_g(R)$ potential curve is obtained by the diagonalization of the field-free Hamiltonian $\hat{T} + V_g(R)$ in the grid representation. The time-dependent n th vibrational-bound-state occupation is

$$P_n^{\text{TSM}}(t) = |\langle \chi_{g,n}(R) | \chi_g(R, t) \rangle|^2. \quad (13)$$

The interaction with the laser field is given in terms of the dipole-coupling matrix elements $d_{gu}(R) = \langle \varphi_u(R; \rho, z) | z | \varphi_g(R; \rho, z) \rangle$ between the two adiabatic electronic states of gerade and ungerade symmetries, $1s\sigma_g$ and $2p\sigma_u$ [39]. The Hamiltonian governing the control-laser pulse interaction can be written in the form

$$\hat{H}_c(R) = \begin{pmatrix} -i\Gamma_g(R, E(t))/2 & d_{gu}(R)E(t) \\ d_{ug}(R)E(t) & -i\Gamma_u(R, E(t))/2 \end{pmatrix}, \quad (14)$$

with isotropic R -dependent molecular ADK rates Γ [40] on the diagonal to account for ionization from both adiabatic electronic states [16, 41].

We obtain the initial coherent vibrational wave packet of the H_2^+ molecular ion at time $t = 0$ by the ionization of the parent H_2 molecule in its vibrational ground state. For simplicity, we assume a Franck–Condon transition and neglect the intensity profile of the pump-laser pulse [42]. The initial vibrational-state distribution $P_n^{\text{TSM}}(0)$ (13) for the singly ionized molecule is shown in the inset of figure 2. We use the same initial-state distribution for both, the 3D and TSM calculations for consistency in this comparison.

2.3. Field-free propagation

As long as there is no interaction with an external field, the 3D calculation (7) and the TSM (11) can be propagated in time analytically. From the knowledge of the complete set of bound eigenfunctions $\psi_n(R, \rho, z)$ and $\chi_{g,n}(R)$, and the corresponding energies E_n^{3D} and E_n^{TSM} , which we obtain by diagonalization of (2) and the field-free Hamiltonian $\hat{T} + V_g(R)$ in (12), respectively, the time evolution is simply given by the phase factor in

$$\Psi(R, \rho, z, t) = \sum_{n=1}^N a_{0,n} \psi_n(R, \rho, z) e^{-iE_n^{\text{3D}} t}, \quad (15)$$

for the 3D calculation, and

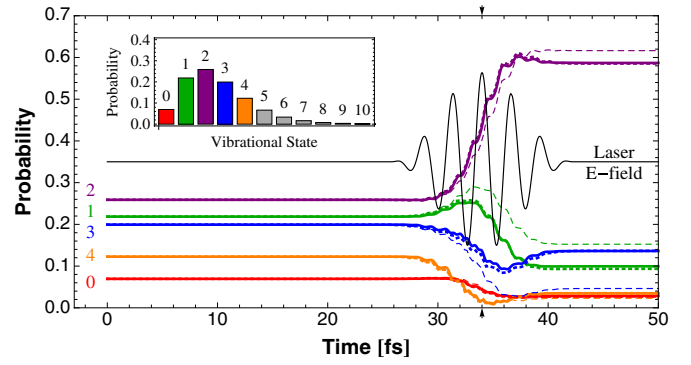


Figure 2. Time evolution of the lowest five vibrational eigenstates of an initial H_2^+ molecular wave packet exposed to a control-laser pulse with a pulse length of 6 fs (FWHM in the intensity), peak intensity of $10^{14} \text{ W cm}^{-2}$, and a central wavelength of 800 nm that is applied at a delay time of 34 fs. Solid lines correspond to 3D calculations, the thin dashed lines to the TSM, and the dotted lines (nearly indistinguishable from the 3D results) show the latter data at a 2% larger control-pulse time delay (see text). The initial vibrational Franck–Condon distribution is shown in the inset. Also shown is the electric field amplitude of the control-laser pulse.

$$\chi_g(R, t) = \sum_{n=1}^N a_{0,n} \chi_{g,n}(R) e^{-iE_n^{\text{TSM}} t}, \quad (16)$$

for the TSM.

The initial probabilities for finding the molecular ion in the n th vibrational eigenstate after the pump pulse are given by the coefficients $|a_{0,n}|^2$.

3. Results

Figure 1 shows TSM results for the change of the vibrational-state amplitudes due to the action of the control pulse. For weak laser intensities the vibrational-state distribution in the electronic ground state would change due to virtual electronic excitations, followed by Stokes and anti-Stokes de-excitations. However, in the present case the laser intensities are sufficiently high for the $2p\sigma_u$ state to become accessible by multi-photon absorption such that the intermediate state in the Raman transition remains populated. The nuclear wave packet can then move on this repulsive potential curve before de-excitation to the $1s\sigma_g$ curve in the control pulse. In general, this leads to the coherent population of a *different* set of vibrational states on the $1s\sigma_g$ curve. The final vibrational-state distribution of the molecule is thus affected by the motion of the wave packet on the repulsive potential curve during the laser pulse. The bandwidth of the 6 fs control-laser pulse in (4) is

$$\Delta\omega = \frac{2\pi}{\beta\tau} = 0.0217, \quad (17)$$

or 0.591 eV. Since the pulse's bandwidth is larger than the typical vibrational level spacing in the hydrogen molecular ion of 0.1–0.3 eV, it allows for Raman transitions to the next nearest vibration states.

3.1. Final vibrational-state distributions in the TSM and full 3D calculations

For a 6 fs control pulse of $10^{14} \text{ W cm}^{-2}$ peak intensity that is applied at a delay time of 34 fs, a significant increase of

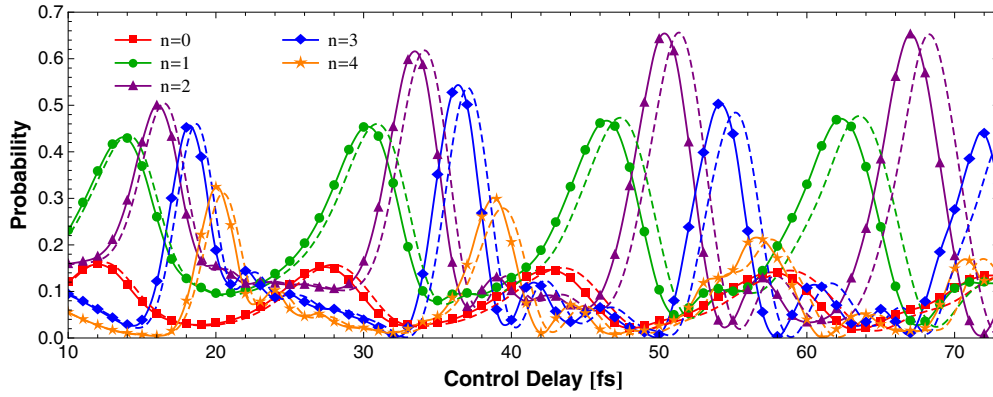


Figure 3. Final vibrational-state probability for the lowest five vibrational eigenstates as a function of the control-pulse delay time. Solid lines correspond to 3D results, while the dashed lines show the TSM. The overall temporal shift between the 3D calculation and the TSM accounts for about 2% of the control-pulse delay for all displayed vibrational states.

Table 1. Final vibrational-state distribution for the lowest six bound vibrational eigenstates for the control-pulse parameters in figure 2 (see text).

n	$P_n^{3D}(\tau)$	$P_n^{TSM}(\tau)$	$P_n^{TSM}(\tau + 2\%)$
0	0.2857	0.2525	0.2726
1	0.0995	0.1524	0.0935
2	0.5869	0.6164	0.5855
3	0.1361	0.0463	0.1366
4	0.0346	0.0227	0.0350
5	0.000 552	0.001 33	0.001 999

Table 2. Energies E_n^{3D} and corresponding classical oscillation times T_n (18) for the first ten bound vibrational states.

n	E_n^{3D} (eV)	T_n (fs)
0	-0.597 40	14.78
1	-0.587 44	15.67
2	-0.578 08	16.65
3	-0.569 30	17.71
4	-0.561 06	18.88
5	-0.553 37	20.19
6	-0.546 19	21.65
7	-0.539 51	23.33
8	-0.533 34	25.27
9	-0.527 66	27.56

the population of a specific vibrational level can be observed. In the example shown in figure 2, the time evolution of the lowest five vibrational eigenstates displays a strong deviation from the initial vibrational-state distribution. The chosen delay maximizes the final contribution of the second vibrational eigenstate. During the interaction with the control-laser pulse, a substantial portion of the population in adjacent vibrational states is transferred into the second vibrational state, thereby more than doubling its initial-state occupancy. The final-state distribution for the given control-pulse parameters is shown in table 1.

The final-state vibrational distribution for the 3D calculations (solid curves) and the TSM (dashed curve) differ slightly in figure 2. This is due to the slightly lower energies E_n^{3D} of the bound vibrational states in the 3D results (15) compared with the TSM energies E_n^{TSM} (16) and leads to a slightly slower oscillating phase factor during the field-free propagation of the wavefunction in the TSM. To correct for this discrepancy, we adjust the initial phase factors for the TSM in (16) to the 3D calculations (15) at the centre of the control pulse. With this adjustment for the phase drift, which corresponds to a shift of about 2% in the control-pulse delay time, both calculations give nearly identical results. The dotted lines in figure 2 show the adjusted TSM results but are nearly invisible because they lie almost on top of the results (thick curves) of the 3D calculation.

3.2. Dependence on the control-pulse delay

To further discuss the observed difference in the two calculations, we compare the final vibrational-state distributions $P_n^{3D}(t \rightarrow \infty)$ and $P_n^{TSM}(t \rightarrow \infty)$ as functions of the control-pulse delay time in figure 3. For the lowest five vibrational eigenstates, the TSM results (dashed curves) are generally stretched in time by about 2% compared to the 3D calculation (solid lines) as noted before. Not including the phase rotations caused by these slightly shifted energies of the eigenstates, the final probabilities in figure 3 almost perfectly overlap for the two calculations.

The periodicity observed in the final-state population for the n th vibrational eigenstate resembles the classical periods [16],

$$T_n = 2 \int_{R_{\min}}^{R_{\max}} dR \sqrt{\frac{M}{2(E_n - V_g(R))}} \quad (18)$$

of a classical particle of energy E_n moving between the two classical turning points R_{\min} and R_{\max} on the $1s\sigma_g^+$ potential curve of the TSM. The corresponding classical vibrational periods T_n for the first few bound vibrational states with energies E_n^{3D} are given in table 2. As can be seen in the table, these values are consistent with the periodicity of the vibrational-state probabilities shown in figure 3 (and figure 5 below). The relevance of the classical oscillation time has also been addressed in the semi-classical treatment reported in [23]. Small differences in T_n can be exploited

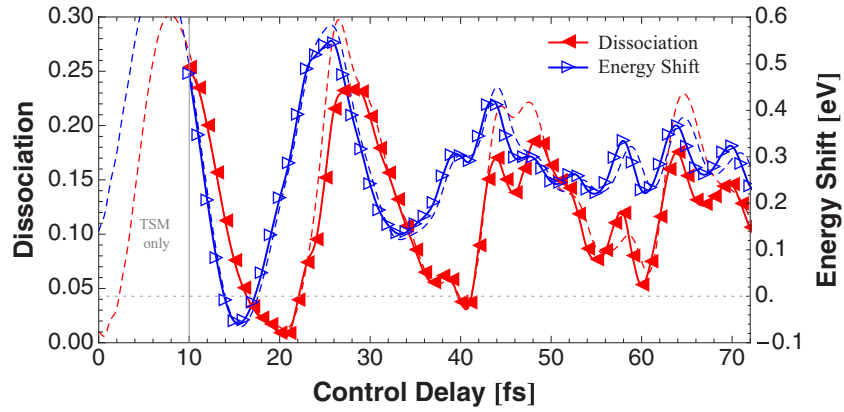


Figure 4. Dissociation probability (red curve with left-pointing filled triangles), and the energetic shift of the remaining bound vibrational wave packet (blue curve with right empty triangles) as a function of the control-pulse delay time. The full-dimensional results are shown by the full curves, while the TSM calculation is indicated through dashed lines. The control-pulse delay has been corrected for the 2% difference in the time evolution for the TSM (see text).

for selecting a desired final vibrational state with a large probability [16, 17, 23], in particular, for the vibrational cooling of the wave packet [25] by reducing its total bound energy.

At a control-laser pulse intensity of 10^{14} W cm $^{-2}$, we find a nearly vanishing contribution to the second ionization of the molecule: the normalization of the wavefunction inside the absorber region of the 3D numerical grid practically does not change during the propagation. This means that the calculated ADK loss rates $\Gamma_g(R, E)$ and $\Gamma_u(R, E)$ in (14) for the TSM remain insignificant at the given maximum electric-field strength. We therefore calculate the dissociation fraction after the control-laser pulse by excluding the probabilities for the nuclei to remain in one of the N lowest vibrational states,

$$P_{\text{diss}}^{\text{3D/TSM}} = 1 - \sum_{n=1}^N P_n^{\text{3D/TSM}}(t_{\text{final}}), \quad (19)$$

for both, the 3D calculation ($P_{\text{diss}}^{\text{3D}}$) and the TSM ($P_{\text{diss}}^{\text{TSM}}$), where the time t_{final} is taken as 10 fs after the control pulse has reached its maximal intensity.

In order to directly compare the dissociation probabilities in figure 4 for the 3D calculation and the TSM, we reduced the control-pulse time delay for the TSM by 2% to account for the slightly lower eigenenergies E_n^{3D} in the 3D calculation. With this adjustment, we generally obtain good agreement for the two simulations. The oscillating vibrational wave packet dissociates more likely when the control pulse occurs at its outer turning point R_{max} [26], where the energy gap between the $1s\sigma_g$ and $2p\sigma_u$ adiabatic electronic states is smaller. This enhancement of the dissociation yield at the outer classical turning point is also seen in the figure. However, the magnitude of the dissociation yield differs slightly in the two calculations when the wave packet reaches R_{max} at 28, 46 and 64 fs. On the other hand, the dissociation probability is almost completely suppressed at a delay time of 20 fs, when the nuclear wave packet returns to the inner turning point R_{min} . This dissociation suppression is also observed for a few more delay times corresponding to multiples of the vibrational period until the wave packet has dephased. The agreement between the two calculations is nearly perfect for small internuclear separations.

3.3. Heating and cooling of vibrational wave packets

To focus on the comparison of the 3D calculation and TSM near the classical turning points, we next discuss the energetic shift of the remaining *bound* wave packet of the molecule after its interaction with the control pulse,

$$\Delta E = \sum_{n=1}^N E_n P_n(t \rightarrow \infty) - E_{\text{initial}}, \quad (20)$$

using E_n^{3D} and E_n^{TSM} for the energies E_n and P_n^{3D} and P_n^{TSM} for the final-state probabilities P_n . The initial energy E_{initial} characterizes the total energy of the initial bound vibrational wave packet in the H_2^+ potential curve immediately following the ionization in the pump pulse from the parent H_2 molecule. As seen in figure 4, the moving nuclear wave packet can be heated by increasing the average energy of the superposition of states close to the outer turning point by promoting the vibrational eigenstates to higher-lying states which extend farther out. However, the maximum of the energy transfer to the molecule occurs before the wave packet reaches the outer turning point, i.e., before the dissociation probability reaches a local maximum. This is caused by competing ‘evaporative cooling’ due to dissociation from the highest occupied vibrational states. This preferential depletion of high-lying vibrational states reduces the total energy of the remaining bound molecule. No second maximum in the vibrational heating can be observed shortly after the dissociation maximum. This suggests that efficient conversion to higher bound vibrational states occurs only for the outwards traveling wave packet. As the wave packet approaches the inner turning point R_{min} vibrational down conversion decreases its energy. This is seen near control-pulse delay times of 16 and 32 fs. At this particular delay, the remaining bound wave packet is dominated by the second vibrational eigenstate, after depletion of $n > 2$ vibrational levels, while the $n = 0$ and $n = 1$ eigenstates remain nearly at their initial population (see figure 3), thereby lowering the total energy of the bound wave packet. Due to dephasing of the nuclear wave packet no further vibrational cooling is observed at moderately larger control-pulse delays, but occurs again near the vibrational revival times at much longer delays. The agreement between

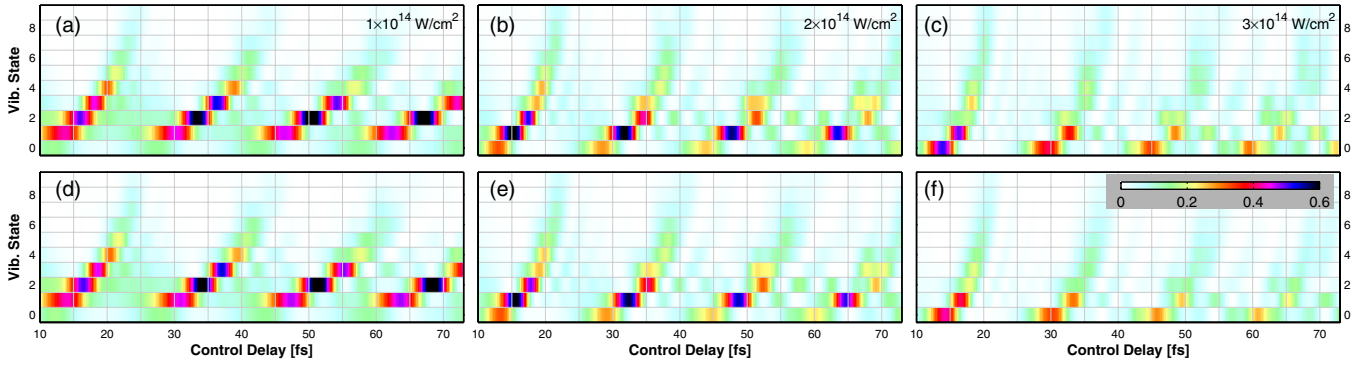


Figure 5. Final H_2^+ vibrational-state distribution after the control pulse as a function of the control-pulse delay time. Top row: results from 3D calculations for control-pulse peak intensities of $10^{14} \text{ W cm}^{-2}$ (left), $2 \times 10^{14} \text{ W cm}^{-2}$ (centre) and $3 \times 10^{14} \text{ W cm}^{-2}$ (right). Bottom row: TSM calculations for the same control-pulse intensities as in corresponding graphs in the top row.

our 3D calculation and the TSM for the shift in energy of the bound wave packet is in general quite good. However, small differences can be observed in particular at the outer classical turning point of the wave packet. Therefore, the TSM works well for the considered parameters and notably differs from the 3D calculation results only for higher-lying vibrational states and in the detailed progression of the dissociation process.

3.4. Dependence of the final vibrational distribution on the control-pulse intensity

We compare our 3D calculation with the TSM in panels (a) and (d) of figure 5, where we display the state-selective final vibrational-state probabilities $P_n(t \rightarrow \infty)$ from (8) and (13) as a function of the control-pulse delay time for a control-pulse peak intensity of $I_0 = 10^{14} \text{ W cm}^{-2}$. For this intensity, the difference between the two vibrational distributions is very small and hardly notable for the entire considered delay range. The small difference is due to the approximately 2% slower propagation in the TSM model that originates, as mentioned above, in the slightly larger vibrational eigenenergies we calculated in the TSM. Otherwise, the TSM describes the final vibrational-state distribution remarkably well and non-adiabatic corrections beyond the $1s\sigma_g-2p\sigma_u$ coupling in the control pulse are irrelevant at the given control-pulse intensity.

While at $I_0 = 10^{14} \text{ W cm}^{-2}$ both calculations result in an almost identical outcome, increasing the control-pulse intensity reveals differences between the 3D and TSM results. To demonstrate this change, we have increased the control-pulse intensity to 2×10^{14} and $3 \times 10^{14} \text{ W cm}^{-2}$ in panels ((b) and (e)) and ((c) and (f)), respectively, of figure 5. By doubling the control-pulse intensity (panels (b) and (e)), clear differences emerge, which become even more pronounced at $3 \times 10^{14} \text{ W cm}^{-2}$ (panels (c) and (f)). In particular, the higher-lying vibrational states are faster depleted in the TSM as compared to the 3D calculation. This agrees with the larger dissociation probability already notable in figure 4 for the TSM at the lower intensity. Whereas for the intermediate intensity and for the lower vibrational states the TSM still agrees well with the 3D calculation, the results differ significantly for the highest intensity shown. Even the lowest vibrational levels become depopulated at $3 \times 10^{14} \text{ W cm}^{-2}$, although the dependence on the control-pulse delay time remains

qualitatively unchanged for the two calculations. Moreover, the increasing control-pulse intensity shows a progressive cooling of the vibrational wave packets into the first excited state (panels (b) and (e)) and the vibrational ground state (panels (c) and (f)) at appropriate control-pulse delays. In the TSM, however, the population of the lowest vibrational levels is underestimated at the highest laser intensity due to the overemphasized ionization probability.

Figure 5 also shows that the increase of the vibrational-state occupation probability in a certain vibrational level only depends on the control-pulse delay time, since the maxima in all six panels appear for the same vibrational level at the same delay time. While the amplitude of the probability-transferring Raman transitions depends, of course, on the control-pulse intensity, the control-pulse delay is decisive for the population transfer into a certain vibration eigenstate. This suggests a unique vibrational quenching scheme, which does not depend on the laser intensity and is robust with regard to the focal volume average in experiments.

Since the final vibrational-state distributions differ increasingly between the TSM calculation and the 3D results for increasing control-pulse intensity, we distinguish the different contributions to dissociation and ionization by fixing the control-pulse delay time at 34 fs and compare the intensity-dependent final distributions (figure 6). For the TSM, the time delay was corrected for the energetic shift by using the same vibrational energies $\{E_n = E_n^{3D}\}$ for the free propagation in (16) as in the 3D calculation (15). The resulting control-pulse intensity dependence of the final vibrational-state distribution is shown for the lowest five vibrational states in figure 6(a). Good agreement at this particular delay time is seen up to an intensity of about $2 \times 10^{14} \text{ W cm}^{-2}$, with the ground-vibrational-state population being correctly described in the TSM up to about $3 \times 10^{14} \text{ W cm}^{-2}$. Also evident is that the second vibrational state remains the preferred quenched state over a large range of laser intensities. The laser intensity where the vibrational quenching starts to become significant is near $6 \times 10^{13} \text{ W cm}^{-2}$, and this vibrational-state selectivity disappears above $2 \times 10^{14} \text{ W cm}^{-2}$. For a control-pulse peak intensity of $1.3 \times 10^{14} \text{ W cm}^{-2}$ the second vibrationally excited-state admixture of the nuclear vibrational wave packet reaches a maximum of 65%. Since the TSM reproduces very well the resulting vibrational-state distribution in this intensity

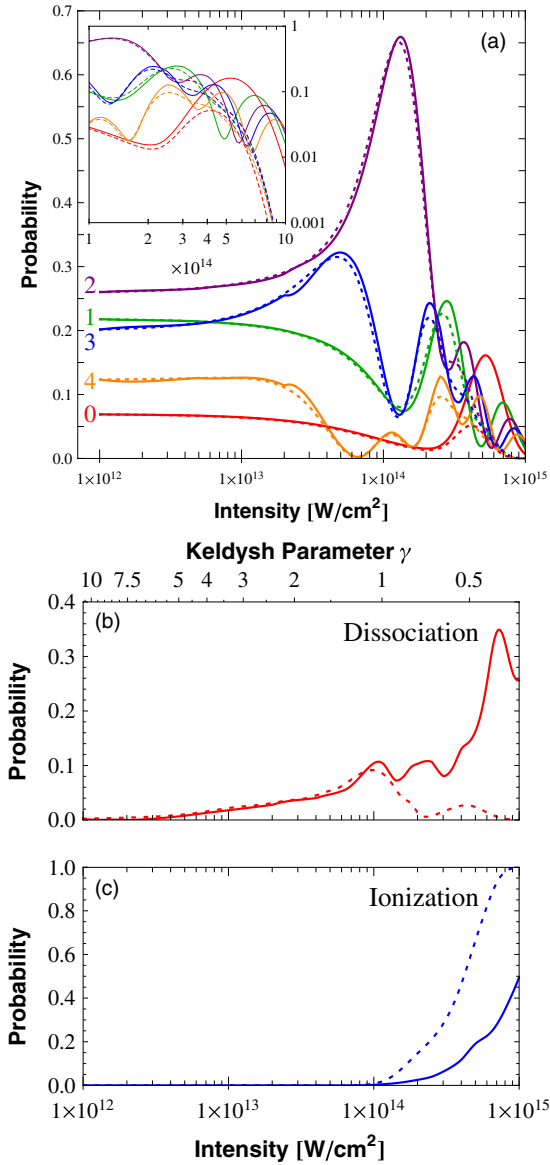


Figure 6. Laser-intensity dependence for the final vibrational-state distribution (a) using a control-pulse delay of 34 fs. Results for 3D calculations (solid lines) and TSM calculations (dashed lines) for the lowest five vibrational eigenstates of H_2^+ whose vibrational quantum numbers are printed to the left of the curves. Total dissociation (b) and ionization (c) probabilities as a function of the control-pulse intensity. In (b) and (c), 3D results are shown as solid lines and TSM results as dashed lines. The Keldysh parameter γ is given on the upper horizontal axis in (b).

range, it can be utilized to find laser parameters that maximize the population in a desired low-lying vibrational eigenstate at low numerical cost.

The total dissociation probability cannot be deduced from the assumption (19) for control-pulse intensities above $10^{14} \text{ W cm}^{-2}$, since ionization no longer remains negligible. At higher intensities, we therefore obtain the ionization probability in our 3D calculations according to

$$P_{\text{ion}} = 1 - \int_{\text{numerical grid}} dR d\rho dz |\Psi(R, \rho, z, t_{\text{final}})|^2, \quad (21)$$

with reference to the remaining probability within the numerical grid at the end of the propagation (10 fs after

the control-pulse maximum). This assumes that the emitted electronic current is absorbed (without numerical reflections) at the grid boundaries, while the nuclear motion is sufficiently slow such that a dissociating wave packet remains inside the numerical box. We tested the convergence of the ionization probability by examining the time dependence of the total norm within the numerical grid after the control pulse. This confirms that even low momentum components of the emitted electron wave packets are absorbed without relevant reflection at the grid boundaries. In this case, the dissociation probability can be calculated according to

$$P_{\text{diss}} = 1 - P_{\text{ion}} - \sum_{n=1}^N P_n(t_{\text{final}}), \quad (22)$$

as the contribution which is neither bound nor leads to ionization. Since this scheme crucially depends on the correct implementation of the wavefunction absorbers at the grid boundaries, we have tested and confirmed numerical convergence by using a series of different absorber parameters. In the TSM, we obtain the total ionization probability by summation over the probabilities for finding the molecular ion in the $1s\sigma_g$ and $2p\sigma_u$ electronic states, governed by the ADK rates $\Gamma_g(R, E(t))$ and $\Gamma_u(R, E(t))$ in (14). The total dissociation probability then follows from (22).

The difference between our two calculations is largely caused by overestimating the ionization process at high control-pulse intensities within the TSM. This is evident in figures 6(b) and (c) that show the dependence of the dissociation (b) and ionization probability (c) on the control-pulse intensity for the fixed delay time of 34 fs. In particular, using molecular ADK depletion rates in the TSM for laser intensities within the tunneling regime above $10^{14} \text{ W cm}^{-2}$ overestimates the ionization probability [41]. Depletion of the bound states due to the dominating ionization process then reduces the observed dissociation yield in the TSM above $1.4 \times 10^{14} \text{ W cm}^{-2}$. Consequently, the TSM only holds for the multi-photon region with Keldysh parameters $\gamma = \sqrt{I_p/2U_p} \gtrsim 1$, where I_p is the ionization potential and U_p the ponderomotive energy in the laser field, as indicated above in figure 6(b), and therefore the TSM needs to be revised for the tunneling region. Thus, the control-pulse intensity of $1.4 \times 10^{14} \text{ W cm}^{-2}$ marks the limit where ionization becomes important, and the TSM starts to fail.

4. Conclusions

We have performed an extensive comparison between our 3D calculations, correctly taking into account non-adiabatic couplings in control laser field, and an adiabatic (Born–Oppenheimer) two-state model (TSM) in which the nuclear motion in H_2^+ is restricted to the $1s\sigma_g$ and $2p\sigma_u$ potential curves. While the qualitative results of both calculations agree remarkably well up to a control-pulse intensity of $10^{14} \text{ W cm}^{-2}$, differences become observable when ionization of the molecular ion starts to become relevant. When ionization is no longer negligible, the explicit inclusion of the electronic degrees of freedom is necessary. Thus, by performing first-principles 3D calculations, we validated

the previously suggested TSM [16] for probe-pulse peak intensities below 10^{14} W cm⁻². In particular, we confirm our earlier prediction of selective vibrational quenching into a given stationary vibrational state for a large range of intensities, providing further evidence for vibrational quenching to be robust against focal volume averaging. In contrast, for control-pulse intensities above 10^{14} W cm⁻², our 3D calculations fail to reproduce the results of the previous TSM due to the participation of higher excited molecular states. We hope, that this work will stimulate a proof-of-principle verification of the vibrational quenching scheme in a future experiment.

The coherent control of the nuclear dynamics examined in this work can be further refined by examining the effect of standardized delayed control pulses on not just the amplitudes $|a_n|$, but also the phases $\arg(a_n)$ in the representation of nuclear wave packets as coherent superpositions of stationary vibrational states (for details see [43]).

Acknowledgments

The authors thankfully acknowledge the computer resources, technical expertise and assistance provided by the Barcelona Supercomputing Center—Centro Nacional de Supercomputación and the Centro de Computación Científica UAM. TN would like to thank Felipe Morales for providing valuable inputs on the use of the PETSc and SLEPs routines. This work was partially supported by the MICINN projects FIS2010-15127, ACI2008-0777 and CSD 2007-00010, the European COST Action CM0702, the ERA-Chemistry project PIM2010EEC-00751, the NSF and the Division of Chemical Sciences, Office of Basic Energy Sciences, Office of Energy Research of the US DOE.

References

- [1] Posthumus J H 2004 *Rep. Prog. Phys.* **67** 623–65
- [2] Lein M 2007 *J. Phys. B: At. Mol. Opt. Phys.* **40** R135–73
- [3] Winter M, Schmidt R and Thumm U 2009 *Phys. Rev. A* **80** 031401
- [4] Winter M, Schmidt R and Thumm U 2010 *New J. Phys.* **12** 023020
- [5] Geltman S 1999 *J. Phys. B: At. Mol. Opt. Phys.* **32** 2309–22
- [6] Palacios A, Bachau H and Martín F 2005 *J. Phys. B: At. Mol. Opt. Phys.* **38** L99–105
- [7] Barmaki S, Bachau H and Ghalim M 2004 *Phys. Rev. A* **69** 043403
- [8] Yarkony D R 1996 *Rev. Mod. Phys.* **68** 985–1013
- [9] Worth G A and Cederbaum L S 2004 *Annu. Rev. Phys. Chem.* **55** 127
- [10] Dundas D, Meharg K J, McCann J F and Taylor K T 2003 *Eur. Phys. J. D* **26** 51–7
- [11] Roudnev V, Esry B D and Ben-Itzhak I 2004 *Phys. Rev. Lett.* **93** 163601
- [12] He F, Becker A and Thumm U 2008 *Phys. Rev. Lett.* **101** 213002
- [13] He F and Becker A 2008 *J. Phys. B: At. Mol. Opt. Phys.* **41** 074017
- [14] Fischer B, Kremer M, Pfeifer T, Feuerstein B, Sharma V, Thumm U, Schröter C D, Moshhammer R and Ullrich J 2010 *Phys. Rev. Lett.* **105** 223001
- [15] Kling M F *et al* 2006 *Science* **312** 246–8
- [16] Niederhausen T and Thumm U 2008 *Phys. Rev. A* **77** 013407
- [17] Murphy D S, McKenna J, Calvert C R, Williams I D and McCann J F 2007 *New J. Phys.* **9** 260
- [18] Vager Z, Naaman R and Kanter E P 1989 *Science* **244** 426–31
- [19] Stapelfeldt H, Constant E, Sakai H and Corkum P B 1998 *Phys. Rev. A* **58** 426–33
- [20] Chelkowski S, Corkum P B and Bandrauk A D 1999 *Phys. Rev. Lett.* **82** 3416–9
- [21] Calvert C R, Birkeland T, King R B, Williams I D and McCann J F 2008 *J. Phys. B: At. Mol. Opt. Phys.* **41** 205504
- [22] Robinett R W 2004 *Phys. Rep.* **392** 1–119
- [23] Bryan W A, Calvert C R, King R B, Nemeth G R A J, Greenwood J B, Williams I D and Newell W R 2010 *New J. Phys.* **12** 073019
- [24] Bryan W A *et al* 2011 *Phys. Rev. A* **83** 021406
- [25] Niikura H, Corkum P B and Villeneuve D M 2003 *Phys. Rev. Lett.* **90** 203601
- [26] Niikura H, Villeneuve D M and Corkum P B 2006 *Phys. Rev. A* **73** 021402
- [27] Calvert C R, Bryan W A, Newell W R and Williams I D 2010 *Phys. Rep.* **49** 1–28
- [28] Bailey D H and Frolov A M 2002 *J. Phys. B: At. Mol. Opt. Phys.* **35** 4287
- [29] Anis F and Esry B D 2008 *Phys. Rev. A* **77** 033416
- [30] Dörner R, Mergel V, Jagutzki O, Spielberger L, Ullrich J, Moshhammer R and Schmidt-Böcking H 2000 *Phys. Rep.* **330** 95–192
- [31] Ullrich J, Moshhammer R, Dorn A, Dörner R, Schmidt L P H and Schmidt-Böcking H 2003 *Rep. Prog. Phys.* **66** 1463–545
- [32] Bromley M W J and Esry B D 2004 *Phys. Rev. A* **69** 053620
- [33] Balay S, Buschelman K, Gropp W D, Kaushik D, Knepley M G, McInnes L C, Smith B F and Zhang H 2009 <http://www.mcs.anl.gov/petsc>
Balay S, Buschelman K, Eijkhout V, Gropp W D, Kaushik D, Knepley M G, McInnes L C, Smith B F and Zhang H 2008 *PETSc Users Manual*, ANL-95/11 - Rev. 3.0.0 (Argonne National Laboratory)
Balay S, Gropp W D, McInnes L C and Smith B F 1997 *Modern Software Tools in Scientific Computing* ed E Arge, A M Bruaset and H P Langtangen (Basel: Birkhäuser) pp 163–202
- [34] Hernandez V, Roman J E and Vidal V 2005 *ACM Trans. Math. Softw.* **31** 351–62 <http://www.grycap.upv.es/slepc>
- [35] Hijikata Y, Nakashima H and Nakatsuji H 2009 *J. Chem. Phys.* **130** 024102
- [36] Press H H, Flannery B P, Teukolsky S A and Vetterling W T 1992 *Numerical Recipes in FORTRAN 77* (Cambridge: Cambridge University Press)
- [37] Thumm U 2002 *Book of Invited Papers: Proc. of 12th ICPEAC (Santa Fe, NM)* (Princeton, NJ: Rinton Press) p 592
- [38] Salin A 1978 *Comput. Phys. Commun.* **14** 121–32
- [39] Kulander K C, Mies F H and Schafer K J 1996 *Phys. Rev. A* **53** 2562
- [40] Ammosov M V, Delone N B and Krainov V P 1986 *Sov. Phys.—JETP* **64** 1191
- [41] Brichta J P, Liu W K, Zaidi A A, Trottier A and Sanderson J H 2006 *J. Phys. B: At. Mol. Opt. Phys.* **39** 3769–79
- [42] Urbain X, Fabre B, Staicu-Casagrande E M, de Ruelle N, Andrianarijaona V M, Jureta J, Posthumus J H, Saenz A, Baldit E and Cornaggia C 2004 *Phys. Rev. Lett.* **92** 163004
- [43] Thumm U, Niederhausen T and Feuerstein B 2008 *Phys. Rev. A* **77** 063401